Giant Enhancement of Magnetic Anisotropy in Ultrathin Manganite Films via Nanoscale 1D Periodic Depth Modulation

A. Rajapitamahuni,[1] L. Zhang,[1] M. A. Koten,[2] V. R. Singh,[1] J. D. Burton,[1] E. Y. Tsymbal,[1,3] J. E. Shield,[2,3] and X. Hong[1,3,*]
[1]*Department of Physics and Astronomy, University of Nebraska–Lincoln, Lincoln, Nebraska 68588-0299, USA*
[2]*Department of Mechanical & Materials Engineering, University of Nebraska–Lincoln, Lincoln, Nebraska 68588-0299, USA*
[3]*Nebraska Center for Materials and Nanoscience, University of Nebraska–Lincoln, Lincoln, Nebraska 68588-0299, USA*

(Received 22 July 2015; revised manuscript received 10 February 2016; published 2 May 2016)

The relatively low magnetocrystalline anisotropy (MCA) in strongly correlated manganites $(\mathrm{La,Sr})\mathrm{MnO_3}$ has been a major hurdle for implementing them in spintronic applications. Here we report an unusual, giant enhancement of in-plane MCA in 6 nm $\mathrm{La_{0.67}Sr_{0.33}MnO_3}$ (LSMO) films grown on (001) $\mathrm{SrTiO_3}$ substrates when the top 2 nm is patterned into periodic stripes of 100 or 200 nm width. Planar Hall effect measurements reveal an emergent uniaxial anisotropy superimposed on one of the original biaxial easy axes for unpatterned LSMO along $\langle 110\rangle$ directions, with a 50-fold enhanced anisotropy energy density of $5.6\times 10^6\ \mathrm{erg/cm^3}$ within the nanostripes, comparable to the value for cobalt. The magnitude and direction of the uniaxial anisotropy exclude shape anisotropy and the step edge effect as its origin. High resolution transmission electron microscopy studies reveal a nonequilibrium strain distribution and drastic suppression in the *c*-axis lattice constant within the nanostructures, which is the driving mechanism for the enhanced uniaxial MCA, as suggested by first-principles density functional calculations.

DOI: 10.1103/PhysRevLett.116.187201

The intricate interplay between the various competing electronic and magnetic orders and the local lattice degree of freedom in strongly correlated oxides, such as the colossal magnetoresistive (CMR) manganites [1], often leads to new ground states and functionalities when these systems are subject to nanoscale structural modification. Notable examples include abrupt resistance switching [2,3], reentrant metal-insulator transitions [4], enhanced ferromagnetic edge states [5], and tunable domain structures [6] in manganite wires and islands. The nanowire approach has also been employed to control the magnetic anisotropy direction in $(\mathrm{La,Sr})\mathrm{MnO_3}$ (LSMO), building on the competition between shape anisotropy and magnetocrystalline anisotropy (MCA) [7].

Bulk LSMO has a uniaxial MCA of $1.8\times 10^4\ \mathrm{erg/cm^3}$ [8], significantly lower than the values for Fe $(4.8\times 10^5\ \mathrm{erg/cm^3})$ and Co $(5\times 10^6\ \mathrm{erg/cm^3})$ [9]. Even though the high spin polarization and CMR effect make LSMO a promising material candidate for magnetic memory, logic, and sensor applications [10–12], the relatively low Curie temperature and magnetic anisotropy have significantly impeded its technological implementation in information storage, with the latter imposing the fundamental limitations on the switching dynamics and thermal stability of the devices. As MCA originates from spin-orbit coupling and is highly sensitive to lattice distortion, it is of both fundamental and technological interests to understand, enhance, and ultimately control the coupling between MCA and the nanoscale structural parameters.

In this Letter, we report an unusual giant enhancement in the in-plane magnetic anisotropy in ultrathin $\mathrm{La_{0.67}Sr_{0.33}MnO_3}$ films when the top layer is patterned into nanoscale periodic stripes. Planar Hall effect (PHE) measurements reveal a strong uniaxial magnetic anisotropy developed along one of the original biaxial easy axes for unpatterned LSMO. The corresponding anisotropy energy density is $\sim 5.6\times 10^6\ \mathrm{erg/cm^3}$ within the nanostripes, comparable to the known value for cobalt. High resolution transmission electron microscopy (HRTEM) studies reveal a large strain gradient within the nanostructures, and first-principles density functional theory calculations suggest that this nonequilibrium strain distribution can account for both the direction and magnitude of the emergent uniaxial MCA. Our work provides new insights into how to manipulate the orbital contribution to MCA in strongly correlated materials through nanostructure engineering. As LSMO is one of the most studied electrode materials for novel spintronic devices such as multiferroic tunnel junctions [12–15], the observed giant uniaxial MCA may facilitate the development of multiferroic-tunnel-junction-based nonvolatile memory applications with enhanced high temperature tunneling resistance and thermal stability.

We deposited high quality epitaxial 6 nm LSMO thin films on (001) $\mathrm{SrTiO_3}$ (STO) substrates using off-axis radio frequency magnetron sputtering [16], and fabricated standard Hall bar structures along the [100] direction with dimensions ranging from 5 to 40 μm [Fig. 1(a)]. We then created in the current channel periodic 2 nm depth modulation using electron beam lithography followed by fluorine-based reactive ion etching (RIE), resulting in 100 or 200 nm wide stripes and trenches along [010] with the width ratio of 1 [Figs. 1(a)–1(c)] [16]. Magnetotransport measurements were carried out using Quantum Design PPMS combined with

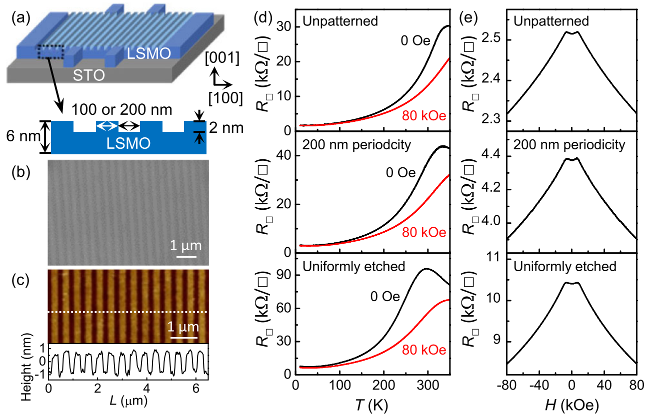

FIG. 1. (a) Schematic views of the nanostructured LSMO Hall bar. (b) SEM image for a 400 nm periodicity nanostructure. (c) AFM topography with the depth profile along the dotted line for a 400 nm periodicity nanostructure. (d) $R_\square(T)$ and (e) $R_\square(H)$ at 100 K for an unpatterned LSMO, a nanostructure with 200 nm periodicity, and a sample uniformly etched to 4 nm.

Keithley 2400 SourceMeter at low excitation currents of 1–10 μA to avoid Joule heating [21]. The reported results are based on 8 nanostructures fabricated on 3 LSMO films.

We first compared the magnetotransport properties of the nanostructured LSMO and two control samples, one unpatterned and one with the entire current channel uniformly etched down to 4 nm. As shown in Figs. 1(d) and 1(e), a nanostructured LSMO with 200 nm periodicity exhibits qualitatively similar temperature and magnetic field dependences of the sheet resistance $R_\square$ as the control samples, indicating that the sample quality is preserved after etching. The progressively higher resistivity, lower resistance peak temperature, and larger magnetoresistance for samples with decreasing average thickness are expected as the films are approaching the electric dead layer thickness (2–3 nm) [21].

For nanostructured samples with small dimensions, magnetization cannot be obtained from direct magnetometry measurements, but can be sensitively probed by magnetotransport techniques such as anisotropic magnetoresistance, PHE, and anomalous Hall effect [22–27]. The PHE is the sinusoidal dependence of the transverse (ρ_{xy}) resistivity on the angle φ between the in-plane magnetization and the current direction [Fig. 2(a)]:

$$\rho_{xy} = (\rho_\parallel - \rho_\perp)\sin\varphi\cos\varphi. \quad (1)$$

Here, $\rho_\parallel$ and $\rho_\perp$ are the resistivity values of a magnetic conductor with the current parallel or perpendicular to magnetization, respectively. Since the PHE signal in LSMO is orders of magnitude larger than that in ferromagnetic metals and not as sensitive to the CMR background as the anisotropic magnetoresistance [24–26], it is an ideal tool for high precision measurement of the magnetization orientation. All PHE measurements were taken at 100 K to achieve optimized signal [16,23,24].

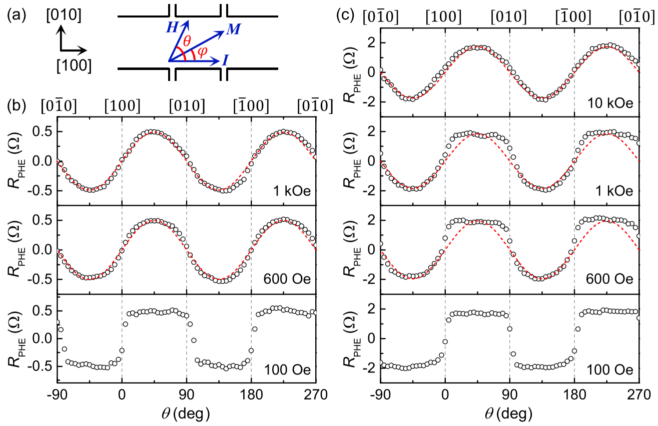

FIG. 2. (a) Schematic measurement setup. $R_{\mathrm{PHE}}(\theta)$ at different magnetic fields for (b) an unpatterned LSMO and (c) a nanostructure with 400 nm periodicity. The dashed lines are the fits to Eq. (1).

Figure 2(b) shows the PHE resistance R_{PHE} for the unpatterned LSMO at different magnetic fields. We first applied an in-plane magnetic field of 6–10 kOe to set the sample in a single domain state, and then measured R_{PHE} at a constant field H while stepping the angle θ it makes with respect to current [Fig. 2(a)]. At high magnetic fields (1 kOe and 600 Oe), magnetization follows the direction of H, and φ can be approximated by θ, yielding sinusoidal $R_{\mathrm{PHE}}(\theta)$ well described by Eq. (1) [Fig. 2(b)]. At lower magnetic fields, magnetic anisotropy becomes progressively important, and φ starts to deviate from θ. At 100 Oe, R_{PHE} exhibits resistance plateaus close to the two peak values over a wide θ range, and only switches abruptly between these two states at $\theta = \pm n\pi/2$. This phenomenon, known as the giant planar Hall effect [23,24], indicates the strong magnetization pinning to one of the in-plane biaxial easy axes along [110] or [1$\bar{1}$0] for LSMO on STO [28–30]. The abrupt resistance switching corresponds to the sharp jump of the magnetization between two easy axes when the magnetic field is swept across the hard axis.

We then examined the PHE in a nanostructure with 400 nm periodicity [Fig. 2(c)]. At 100 Oe, we observe the giant planar Hall effect qualitatively similar to those in unpatterned LSMO, indicating the existence of biaxial anisotropy. At 600 Oe, above the anisotropy field for unpatterned LSMO, R_{PHE} recovers the sinusoidal θ dependence in the vicinity of $\theta = -45°$ and 135°. In sharp contrast, close to $\theta = 45°$ and 225°, the wide resistance plateaus still persist, and survive at magnetic fields well above 1 kOe, pointing to a much stronger pinning of magnetization along the [110] and [$\bar{1}\,\bar{1}$0] directions. At 10 kOe, R_{PHE} fully restores the sinusoidal θ dependence.

The striking difference in how $R_{\mathrm{PHE}}(\theta)$ evolves with the magnetic field clearly indicates the different anisotropy energy landscapes in the unpatterned and nanostructured LSMO. The total free-energy density can be understood within the Stoner-Wohlfarth model [9]:

$$F = K_u \sin^2\left(\varphi - \frac{\pi}{4}\right) + \frac{K_1}{4}\sin^2 2\left(\varphi - \frac{\pi}{4}\right) - MH\cos\left(\varphi - \theta\right). \tag{2}$$

Here, K_u and K_1 are the uniaxial and biaxial magnetic anisotropy constants, with K_u negligibly small for unpatterned LSMO on STO [29]. The last term denotes the Zeeman energy associated with the magnetization M. This model assumes coherent rotation of a single domain state, which is reasonable given the small dimensions of our samples [31]. The critical condition for the transition from the low field ($\varphi \neq \theta$) regime to the high field ($\varphi \approx \theta$) regime cannot be solved analytically, but can be well approximated by the biaxial and uniaxial anisotropy fields H_1 and H_u with $H_{1,u} = 2K_{1,u}/M$ [9,23].

To quantitatively identify the anisotropy fields, we extracted the angle φ from the normalized R_{PHE} using $\varphi = \frac{1}{2}\sin^{-1}(R_{\mathrm{PHE}}/R_{\mathrm{PHE,max}})$ [Eq. (1)]. Figure 3(a) shows $\varphi(\theta)$ at different magnetic fields within the $\theta = [-45°, 45°]$ quadrant, where φ exhibits strong pinning to ±45° for the unpatterned LSMO at low fields and only to +45° for the nanostructured LSMO at intermediate fields. The nonlinearity of $\varphi(\theta)$ diminishes with increasing magnetic field, which was quantified by calculating the residual sum of squares of the linear fit: $\mathrm{RSS} = \sum_i [\varphi(\theta_i) - \theta_i]^2$. For all samples, *RSS* decreases rapidly with increasing H and tends to saturate at a critical magnetic field [Figs. 3(b) and 3(c)], which we use to approximate the anisotropy field.

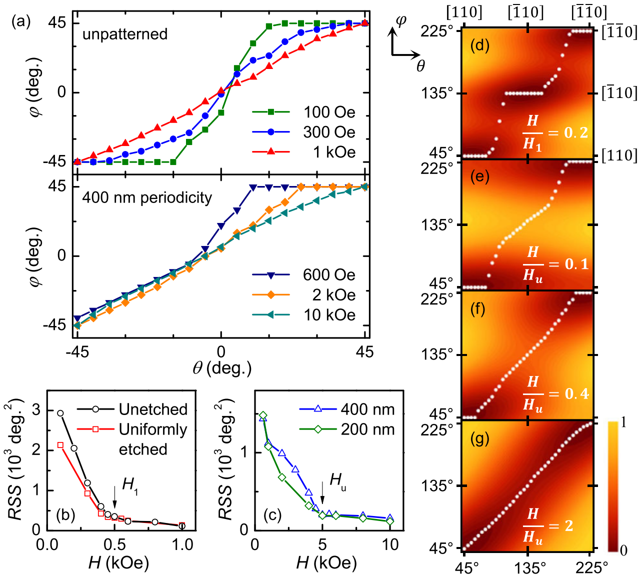

FIG. 3. (a) Extracted φ versus θ at different magnetic fields for the unpatterned and nanostructured samples shown in Fig. 2. (b) *RSS* versus H for the unpatterned LSMO and 4 nm uniformly etched LSMO. (c) *RSS* versus H for the LSMO nanostructures with 400 and 200 nm periodicities. (d)–(g) Normalized free-energy landscape versus φ and θ at different magnetic fields [Eq. (2)]: (d) considers only the biaxial anisotropy; (e)–(g) consider only the uniaxial anisotropy. Superimposed white dots are the extracted $\varphi(\theta)$ data for the nanostructured sample shown in (a) at magnetic fields of 100 Oe, 500 Oe, 2 kOe, and 10 kOe, respectively.

For the unpatterned LSMO, $H_1 \approx 500$ Oe [Fig. 3(b)]. Assuming the lattice parameters of a fully strained film, our ultrathin LSMO possesses a magnetization of 3.16 μ_B/Mn at 10 K [16]. Using $H_1 = 2K_1/M$ and the magnetization measured at 100 K (2.81 μ_B/Mn), we find the biaxial anisotropy energy density to be 1.1×10^5 erg/cm^3, comparable to previously reported values for LSMO on STO [8,29–31]. The PHE in the uniformly etched 4 nm sample exhibits qualitatively similar field dependence [16] with a similar anisotropy field of $H_1 \approx 500$ Oe [Fig. 3(b)], confirming that the unusual enhancement of anisotropy is not due to chemical modification of the sample surface during etching.

For the nanostructured sample, the *RSS* diminishes around $H_u \approx 5000$ Oe, one order of magnitude higher than H_1. It is important to note that we only expect the magnetic anisotropy within the nanostripes being modulated. The continuous base layer should exhibit biaxial anisotropy as the unpatterned thin films, and its magnetization rotation is solely driven by that of the top nanostructures, assuming a single domain state of the entire sample. The measured anisotropy field H_u is thus related to the nanostructure anisotropy energy density K_u as $H_u = (2K_u/M)(V_{\mathrm{stripe}}/V_{\mathrm{total}})$, where $(V_{\mathrm{stripe}}/V_{\mathrm{total}}) = 0.2$ is the volume ratio between the stripe region and the entire sample [Fig. 1(a)]. The corresponding uniaxial anisotropy K_u is 5.6×10^6 erg/cm^3, about 50 times larger than the biaxial MCA in unpatterned LSMO. Taking the magnetic dead layer into account does not yield a significant change to K_u [16].

To better visualize the energy competition between the magnetic anisotropy and the Zeeman energy, we plot in Figs. 3(d)–3(g) the simulated energy contour versus φ and θ based on Eq. (2) at different ratios of $H/H_{1,u}$. Figure 3(d) considers only the biaxial magnetic anisotropy with $H/H_1 = 0.2$, and Figs. 3(e)–3(g) consider only the uniaxial magnetic anisotropy with $H/H_u = 0.1$, 0.4, and 2, respectively. Superimposed on the simulations are the extracted φ *versus* θ data for the nanostructured sample at $H = 100$ Oe, 500 Oe, 2 kOe, and 10 kOe, respectively. Here the locus of $\varphi(\theta)$ agrees well with the local energy minima and crosses the energy barriers (magnetic hard axes) through the saddle points. The disappearance of the plateau located at $\varphi = 135°$ at 500 Oe [Fig. 3(e)] and the linear $\varphi(\theta)$ relation at 10 kOe [Fig. 3(g)] are in excellent agreement with the simulated energy landscapes, indicating that the extracted H_1 and H_u give an accurate description of the magnetic anisotropy energies (MAE) in the system.

To confirm the robustness of the effect, we investigated 5 nanostructures with 400 nm periodicity and 3 nanostructures with 200 nm periodicity [16]. Statistical analysis shows that the anisotropy field does not show apparent dependence on the periodicity of the nanostructure. For all nanostructures characterized at high fields, H_u is in the

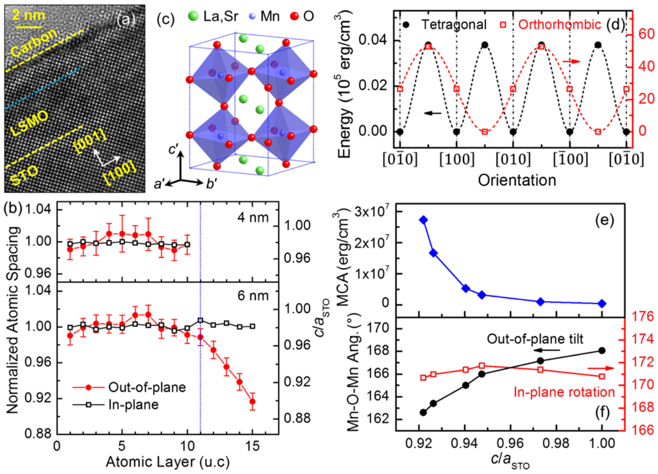

FIG. 4. (a) Cross-sectional HRTEM micrograph of a nanostructured LSMO, with the film surface or interface (dashed lines) and the top boundary of the 4 nm base layer (dotted line) highlighted. (b) Normalized atomic spacing (left axis) and the corresponding c/a_{STO} ratio (right axis) as a function of distance from the STO interface. AL 1 is right at the interface. The errors for the in-plane values are ∼0.3%. The data for the topmost surface AL cannot be reliably deduced due to the presence of the amorphous carbon cap layer and are not shown. (c) Schematic view of the orthorhombic LSMO unit cell, with a' and b' 45° rotated from the pseudocubic crystal axes. (d) Calculated magnetic energy as a function of in-plane orientation for tetragonal and orthorhombic LSMO with $c/a_{\mathrm{STO}} = 0.94$. The dashed lines are sinusoidal fits. (e) Calculated MCA and (f) the $\mathrm{MnO_6}$ tilt and rotation angles for the orthorhombic LSMO as a function of c/a_{STO}.

range of 4750–5000 Oe [Fig. 3(c)]. In addition, the induced uniaxial easy axes can be along either [110] or [1$\bar{1}$0], indicating that the preferred axis is not controlled in our current experimental setup.

There are several mechanisms that can modify the direction and magnitude of magnetic anisotropy in LSMO, including magnetostatic energy induced shape anisotropy [7], step edge effects [31,32], and epitaxial strain [8,28–30]. Shape anisotropy and step edge effects can be ruled out as possible origins based on three observations. First, both scenarios predict an induced uniaxial anisotropy along the stripe or trench direction ([010]), while the observed anisotropy is along ⟨110⟩. Second, neither scenario can account for the large magnitude of the effect. Quantitative analysis of the geometry of the depth modulation yields a shape anisotropy of 4×10^4 to 7×10^4 erg/cm^3 [16,33]. The step edge effect gives rise to a uniaxial anisotropy of similar magnitude, as observed in LSMO grown on vicinal STO substrates [31,32]. Third, in both scenarios, the induced uniaxial anisotropies are geometry dependent, scaling with the width-to-height ratio or step edge density of the stripe structures [31–34]. The nanostructured LSMO with 400 and 200 nm periodicities have identical volume fractions for the stripe regions (50% of the top 2 nm layer), while both the width-to-height ratios and the step edge densities differ by a factor of 2. The fact that they possess identical anisotropy energy densities within the expected fluctuation due to lithography (dimension variation <10%) strongly points to a bulk effect associated with modified MCA, rather than a surface or edge effect, as its origin.

To identify the structural origin of the enhanced MCA, we carried out HRTEM studies of the nanostructured samples [Fig. 4(a)] [16], from which we extracted the out-of-plane and in-plane lattice constants of LSMO as a function of distance from the interface with STO. For both the 6 nm region that hosts the nanostripes and the 4 nm etched areas, there is no apparent variation in the in-plane lattice constants from that of STO (a_{STO}), showing that the nanostructured sample is fully strained to the substrate [Fig. 4(b)]. In sharp contrast, a gradual reduction of the out-of-plane lattice constant occurs in the top 4–5 atomic layers (ALs) of the 6 nm region, which is within the nanostripe region, leading to a drastic suppression of the c/a ratio from 0.98 for the unpatterned area to 0.9 close to the surface layers. Such a nonequilibrium strain distribution is absent in the 4 nm region [Fig. 4(b)], and is likely stabilized due to the lack of lateral boundary confinement for the nanostripes.

To gain microscopic understanding of the impact of such a large strain, we performed first-principles density functional theory calculations of bulk LSMO with a and b axes uniformly strained to STO and different enforced c values [16,35]. As the in-plane lattice of the nanostructure is fully strained to STO, it can only take the tetragonal or orthorhombic distortion. To account for the observed in-plane uniaxial anisotropy, which requires breaking the symmetry between the pseudocubic [110] and [1$\bar{1}$0] directions, we employed an orthorhombic structure with *Imma* space group, with the underlying orthorhombic symmetry being characterized by tilting the $\mathrm{MnO_6}$ octahedral along the pseudocubic [110] direction [Fig. 4(c)]. We then included spin-orbit coupling in these strained bulk structures to determine the MAE. Figure 4(d) shows the calculated magnetic energies for the tetragonal and orthorhombic distortion as a function of the in-plane magnetization orientation for strained LSMO with $c/a_{\mathrm{STO}} = 0.94$, which is the average strain level for the nanostructure. While the tetragonal distortion gives rise to a weak biaxial anisotropy of 3.80×10^3 erg/cm^3 along the [100] and [010] directions, a uniaxial anisotropy of 5.28×10^6 erg/cm^3 can be established along the [110] direction for the orthorhombic structure, comparable with the experimentally extracted value of 5.6×10^6 erg/cm^3.

Our simple bulk calculations combined with experimental lattice parameters have thus successfully captured both the direction and magnitude of the emergent uniaxial MCA. The drastic suppression of the c-axis lattice constant can only be stabilized due to the presence of the nonequilibrium strain distribution within the nanostructure. This model also naturally explains why such an enhancement was not observed in the previous nanowire studies based on thick

LSMO layers, where the structure is likely relaxed [7]. The bulk calculations further show that the MCA increases monotonically with decreasing c/a_{STO} ratio, approaching 2.7×10^7 erg/cm^3 at $c/a_{\mathrm{STO}}=0.92$ [Fig. 4(e)], and point to the critical role of the out-of-plane $\mathrm{MnO_6}$ tilt in controlling the in-plane MCA. Figure 4(f) shows the Mn-O-Mn angle for the $\mathrm{MnO_6}$ octahedral as a function of c/a_{STO}. While the in-plane rotation angle only exhibits moderate change for the entire strain range, the out-of-plane $\mathrm{MnO_6}$ tilt angle decreases from 168.1° at $c/a_{\mathrm{STO}}=1$ to 162.6° at $c/a_{\mathrm{STO}}=0.92$, with an accelerated change occurring right at $c/a_{\mathrm{STO}}=0.94$, concurrent with the sharp rise of the MCA. Such high sensitivity of manganites to the $\mathrm{MnO_6}$ distortion can thus be utilized as a powerful tool to tailor their electronic and magnetic states at the nanoscale [25–27,36–38].

In conclusion, we have demonstrated a 50-fold enhancement of magnetic anisotropy in LSMO via nanostructure engineering. Our work reveals the critical role of local lattice strain in controlling MCA in strongly correlated oxides, which points to a novel route for imposing designed magnetic functionalities into complex oxide thin films and interfaces, paving the path for their application in nanoelectronic and spintronic applications.

We would like to thank Xiaoshan Xu, Sai Mu, and Balamurugan Balasubramanian for insightful discussions and technical assistance, Sy-Hwang Liou for the access to the RIE, and David Sellmyer for the access to the SQUID. This work was supported by the Nebraska Materials Research Science and Engineering Center (MRSEC) (NSF Grant No. DMR-1420645) (structural characterizations and theoretical modeling), NSF CAREER Grant No. DMR-1148783 (magnetic and electrical characterizations), and the Nanoelectronics Research Corporation (NERC), a wholly owned subsidiary of the Semiconductor Research Corporation (SRC), through the Center for Nanoferroic Devices (CNFD), an SRC-NRI Nanoelectronics Research Initiative Center under Task ID 2398.002 (sample growth and device fabrication). Part of the research utilized the central facilities of the Nebraska Center for Materials and Nanoscience, which is supported by the Nebraska Research Initiative. Computations were performed at the Holland Computing Center of the University of Nebraska–Lincoln.

A. R. and L. Z. contributed equally to this work.

---

[*] Corresponding author.
xhong2@unl.edu

[1] Y. Tokura, *Colossal Magnetoresistive Oxides* (CRC Press, Boca Raton, 2000).

[2] H. Y. Zhai, J. X. Ma, D. T. Gillaspie, X. G. Zhang, T. Z. Ward, E. W. Plummer, and J. Shen, Phys. Rev. Lett. **97**, 167201 (2006).

[3] G. Singh-Bhalla, S. Selcuk, T. Dhakal, A. Biswas, and A. F. Hebard, Phys. Rev. Lett. **102**, 077205 (2009).

[4] T. Z. Ward, S. Liang, K. Fuchigami, L. F. Yin, E. Dagotto, E. W. Plummer, and J. Shen, Phys. Rev. Lett. **100**, 247204 (2008).

[5] K. Du, K. Zhang, S. Dong, W. Wei, J. Shao, J. Niu, J. Chen, Y. Zhu, H. Lin, X. Yin, S.-H. Liou, L. Yin, and J. Shen, Nat. Commun. **6**, 6179 (2015).

[6] Y. Takamura, R. V. Chopdekar, A. Scholl, A. Doran, J. A. Liddle, B. Harteneck, and Y. Suzuki, Nano Lett. **6**, 1287 (2006).

[7] M. Mathews, R. Jansen, G. Rijnders, J. C. Lodder, and D. H. A. Blank, Phys. Rev. B **80**, 064408 (2009).

[8] Y. Suzuki, H. Y. Hwang, S. W. Cheong, T. Siegrist, R. B. van Dover, A. Asamitsu, and Y. Tokura, J. Appl. Phys. **83**, 7064 (1998).

[9] C. Tannous and J. Gieraltowski, Eur. J. Phys. **29**, 475 (2008).

[10] Y. Bason, L. Klein, J. B. Yau, X. Hong, J. Hoffman, and C. H. Ahn, J. Appl. Phys. **99**, 08R701 (2006).

[11] J. Hoffman, X. Hong, and C. H. Ahn, Nanotechnology **22**, 254014 (2011).

[12] M. Bibes, J. Villegas, and A. Barthelemy, Adv. Phys. **60**, 5 (2011).

[13] E. Y. Tsymbal and H. Kohlstedt, Science **313**, 181 (2006).

[14] E. Y. Tsymbal, A. Gruverman, V. Garcia, M. Bibes, and A. Barthelemy, MRS Bull. **37**, 138 (2012).

[15] Y. W. Yin, J. D. Burton, Y. M. Kim, A. Y. Borisevich, S. J. Pennycook, S. M. Yang, T. W. Noh, A. Gruverman, X. G. Li, E. Y. Tsymbal, and Q. Li, Nat. Mater. **12**, 397 (2013).

[16] See Supplemental Material at http://link.aps.org/supplemental/10.1103/PhysRevLett.116.187201 for supporting information, which includes Refs. [17–20].

[17] C. A. Schneider, W. S. Rasband, and K. W. Eliceiri, Nat. Methods **9**, 671 (2012).

[18] P. Giannozzi *et al.*, J. Phys. Condens. Matter **21**, 395502 (2009).

[19] J. P. Perdew, K. Burke, and M. Ernzerhof, Phys. Rev. Lett. **77**, 3865 (1996).

[20] P. G. Radaelli, G. Iannone, M. Marezio, H. Y. Hwang, S. W. Cheong, J. D. Jorgensen, and D. N. Argyriou, Phys. Rev. B **56**, 8265 (1997).

[21] V. R. Singh, L. Zhang, A. K. Rajapitamahuni, N. Devries, and X. Hong, J. Appl. Phys. **116**, 033914 (2014).

[22] H. Ohno, D. Chiba, F. Matsukura, T. Omiya, E. Abe, T. Dietl, Y. Ohno, and K. Ohtani, Nature (London) **408**, 944 (2000).

[23] H. X. Tang, R. K. Kawakami, D. D. Awschalom, and M. L. Roukes, Phys. Rev. Lett. **90**, 107201 (2003).

[24] Y. Bason, L. Klein, J. B. Yau, X. Hong, and C. H. Ahn, Appl. Phys. Lett. **84**, 2593 (2004).

[25] X. Hong, J. B. Yau, J. D. Hoffman, C. H. Ahn, Y. Bason, and L. Klein, Phys. Rev. B **74**, 174406 (2006).

[26] D. Preziosi, I. Fina, E. Pippel, D. Hesse, X. Marti, F. Bern, M. Ziese, and M. Alexe, Phys. Rev. B **90**, 125155 (2014).

[27] X. Hong, J. Phys. Condens. Matter **28**, 103003 (2016).

[28] P. Lecoeur, P. L. Trouilloud, G. Xiao, A. Gupta, G. Q. Gong, and X. W. Li, J. Appl. Phys. **82**, 3934 (1997).

[29] K. Steenbeck and R. Hiergeist, Appl. Phys. Lett. **75**, 1778 (1999).

[30] F. Tsui, M. C. Smoak, T. K. Nath, and C. B. Eom, Appl. Phys. Lett. **76**, 2421 (2000).

[31] Z. H. Wang, G. Cristiani, and H. U. Habermeier, Appl. Phys. Lett. **82**, 3731 (2003).

[32] M. Mathews, F. M. Postma, J. C. Lodder, R. Jansen, G. Rijnders, and D. H. A. Blank, Appl. Phys. Lett. **87**, 242507 (2005).

[33] E. Y. Tsymbal, Appl. Phys. Lett. **77**, 2740 (2000).

[34] D. S. Chuang, C. A. Ballentine, and R. C. O'Handley, Phys. Rev. B **49**, 15084 (1994).

[35] J. D. Burton and E. Y. Tsymbal, Phys. Rev. Lett. **106**, 157203 (2011).

[36] A. Vailionis, H. Boschker, W. Siemons, E. P. Houwman, D. H. A. Blank, G. Rijnders, and G. Koster, Phys. Rev. B **83**, 064101 (2011).

[37] F. Sandiumenge, J. Santiso, L. Balcells, Z. Konstantinovic, J. Roqueta, A. Pomar, J. P. Espinós, and B. Martínez, Phys. Rev. Lett. **110**, 107206 (2013).

[38] J. M. Rondinelli, S. J. May, and J. W. Freeland, MRS Bull. **37**, 261 (2012).